L. Gagnon[1]*, M. J. Richard*[1]*, P. Masarati*[2]*, M. Morandini*[2]*, and G. Doré*[3]

An Implicit Rigid Ring Tire Model for Multibody Simulation with Energy Dissipation

ABSTRACT: A rigid ring tire model was developed as the c++ module of a free multibody dynamics software. It takes as input the longitudinal profile of the road and attaches to the wheel element of a multibody simulation. It is intended to evaluate the transient behavior of the tire rolling on a deteriorated road profile. It is tailored for, but not restricted to, applications at low camber angles, limited steering and velocity changes, and continuous contact with the road. It is expected to be accurate under excitation frequencies up to 100 Hz and road deformation up to 10 cm. It takes 45 tire parameters and 20 algorithm parameters and is integrated implicitly except for the road profile. The model has been calibrated and validated against a trusted finite element analysis of Michelin XZA-3 tires mounted on a wheel and axle assembly going over rectangular cleats. The resulting curves showed good agreement with the finite element data. The Nelder-Mead optimization process used on the manually determined parameters was able to increase the average coefficient of determination of the twelve test curves from -0.4 to 0.6. Over 20 km/h, that coefficient was above 0.8 for every test of the vertical force response to cleats. As for the longitudinal forces, only one curve had a coefficient below 0.5. A variable timestep algorithm was also included in the module and found to reduce the simulation time of the test cases by roughly 85%.

A class 8 semi-trailer truck model was needed as part of a project that will evaluate influence of the road surface irregularities on the efficiency of transportation. The multibody dynamics method was chosen because it is reliable for solving vehicle dynamics problems. Particular attention was to be given to fuel consumption, contact forces with the ground, and vibrations. These requirements call for an accurate as feasible tire modeling and thus a particular attention was given to the tire model. It should solve quickly for trucks going over long straight and mostly flat stretches of roads having various degradation levels.

Simple yet widely used tire models tend to rely solely on steady-state friction data. However, Canudas and Tsiotras [3] pointed out the generally accepted fact that transient and steady-state friction responses are quite different. At the other end of the spectrum, finite element models are very precise and can even predict the distribution of contact stresses on the tire [24]. However, they do not solve quickly enough to use them in the multibody simulation and they provide more

[1]Département de Génie Mécanique, Université Laval, 1065, de la Médecine, Québec (QC) G1V 0A6 Canada
[2]Dipartimento di Ingegneria Aerospaziale, Politecnico di Milano, Via La Masa 34, 20156 Milano, Italia
[3]Département de Génie Civil, Université Laval, 1065, de la Médecine, Québec (QC) G1V 0A6 Canada

data than is needed. In between those two approaches are the rigid ring tire models. They have the ability to transmit driving and braking torque from the wheel to the ground and were used by different authors such as Pacejka [16], Zegelaar [25], Maurice [13], Besselink [2], Schmeitz [19], Allen [8], Frey [5], and Maas [9]. Each of them concludes that rigid ring models are the best available non finite element models for the analysis of the dynamic response of tires on irregular road profiles. The previously mentioned authors do not cover much on the energy dissipation of tires. Nevertheless, Miège and Popov [15] reviewed the literature and compared the ability of various tire models to predict energy dissipation incurred by road irregularities. While not having specifically tested rigid ring models, they concluded that models using springs and dampers were the best candidates for the purpose. They stated so based on their comparison of various models with the experimental data of Popov *et al.* [17] for excitation frequencies below 5 Hz. Their conclusion so far is that the road surface irregularities have no influence on the rolling resistance within the frequency range considered, and this phenomenon is explainable by the fact that a rotating tire will undergo deformations regardless of whether it encounters a cleat or not on its path. Alternatively, Velinsky and White [23] rather report that road surface irregularities are widely known to affect tire rolling resistance. Both Miège and Popov [15] and Velinsky and White [23] do conclude that the dissipative effects of tires operating on irregular roads are still not well understood. It is assumed here that, if a model can accurately predict dynamic forces and moments on the axle while also relying on springs and dampers, it should consequently accurately predict energy dissipation.

It was thus chosen to implement a rigid ring tire model into the free software *MBDyn* [1]. It is largely based on the *Short Wavelength Intermediate Frequency Tire* (SWIFT) model presented by Pacejka [16] and the road filtering used by Schmeitz [19]. The multibody inputs to the model consist of the three-dimensional forces and moments coming from the wheel and a two-dimensional road profile height defined from a function of position. The model equations are implicitly integrated at each time step and the rotation parameters are handled by the updated-updated approach defined by Masarati [10].

A simplified physical interpretation of the model is shown in Fig. 1. It has three rigid elements. The central element is referred to as the wheel and comprises the wheel and any rotating mass attached to it, including a portion of the tire sidewall. The outer element is referred to as the ring and represents part of the sidewall, the belt, and the tread of the tire and its purpose is to simulate the inertia of a

rotating tire. The remaining rigid element is a point mass referred to as the patch and represents the translational inertia of the portion of the tread which exchanges friction and constraining forces with the ground. There are three independent translational viscoelastic elements that link the wheel to the ring and three that link the ring to the patch. There are also three independent torsional viscoelastic elements that link the wheel to the ring. The deformable elements that join the wheel to the ring are called the carcass elements while the ones that join the ring to the patch are called the residual elements. The patch is not subjected to gravity. Its height is dictated by its longitudinal position on the road and its vertical velocity is determined from the following relationship,

$$v_{\mathrm{p3}} = -v_1 \frac{\hat{\boldsymbol{n}} \cdot \hat{\mathbf{i}}}{\hat{\boldsymbol{n}} \cdot \hat{\mathbf{k}}} \tag{1}$$

The empirical formulae published by Pacejka [16] are used to obtain the slip forces to be applied on that patch. The tire inflation pressure used throughout the article is 7.9 bar.

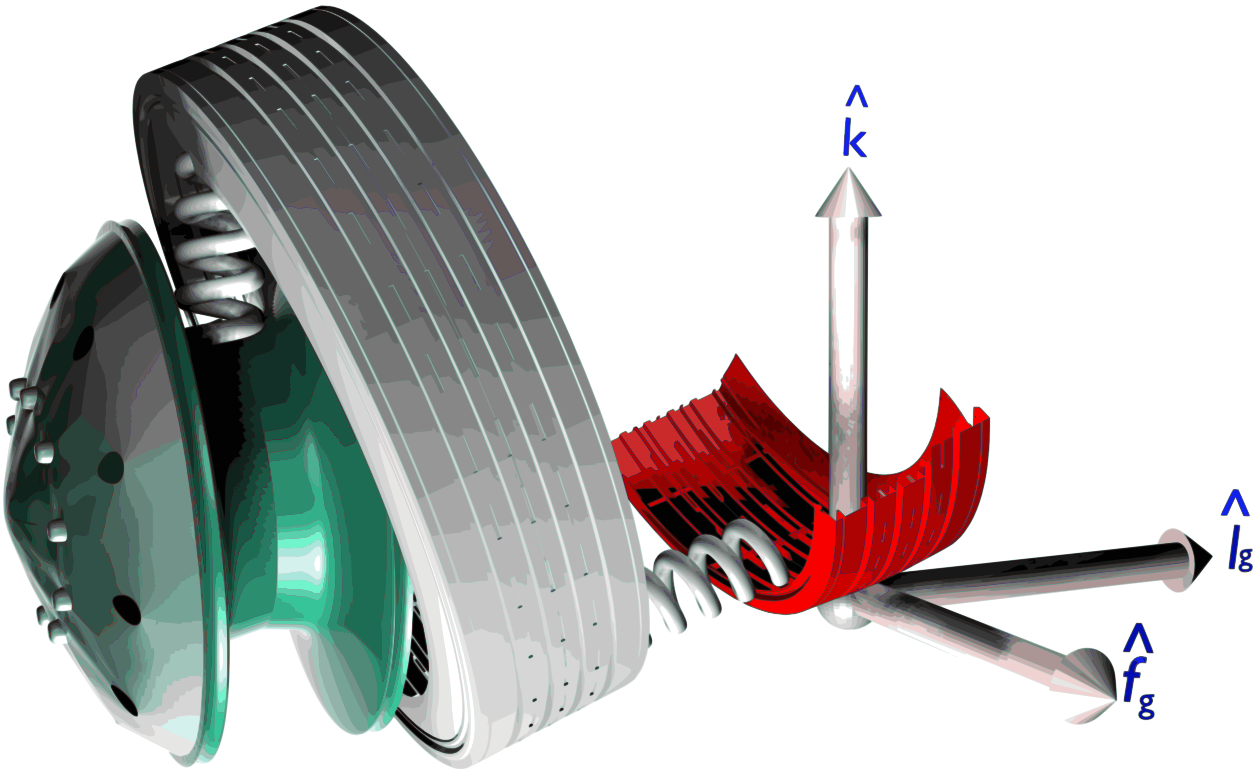

Figure 1: From left to right: wheel, ring, and patch elements.

1 Notation and Definitions

Vectors and matrices are expressed by bold lowercase and uppercase characters, respectively. Vector are defined as row vectors and the exponent T indicates a transposition to a column vector. The $\odot$ operator represents an element-by-element multiplication. Variables are italicized and constants are straight. Unit vectors codirectional to the main axes are $\hat{\mathbf{i}} = \begin{bmatrix}1 & 0 & 0\end{bmatrix}$, $\hat{\mathbf{j}} = \begin{bmatrix}0 & 1 & 0\end{bmatrix}$, and $\hat{\mathbf{k}} = \begin{bmatrix}0 & 0 & 1\end{bmatrix}$. The vectors $\boldsymbol{x}_\mathrm{i}$, $\boldsymbol{v}_\mathrm{i}$, and $\boldsymbol{\omega}_\mathrm{i}$ represent the position, velocity, and angular velocity of element i, respectively, where the subscripts w, r, and p refer to the wheel, ring, and patch, respectively. The rotation matrix of element i is expressed by $\boldsymbol{R}_\mathrm{i}$. The unit vectors in the forward and lateral direction of element i are $\hat{\boldsymbol{f}}_\mathrm{i} = \frac{(\boldsymbol{R}_\mathrm{i}\hat{\boldsymbol{a}})\times\hat{\boldsymbol{n}}}{|(\boldsymbol{R}_\mathrm{i}\hat{\boldsymbol{a}})\times\hat{\boldsymbol{n}}|}$ and $\hat{\boldsymbol{l}}_\mathrm{i} = \hat{\boldsymbol{n}} \times \hat{\boldsymbol{f}}_\mathrm{i}$, respectively and where $\hat{\boldsymbol{a}}$ is the axle unit direction vector with respect to the ring. Modified ring unit vectors, which behave as if there were no slope on the road profile, are given by $\hat{\boldsymbol{f}}_\mathrm{g} = \frac{(\boldsymbol{R}_\mathrm{r}\hat{\boldsymbol{a}})\times\hat{\mathbf{k}}}{|(\boldsymbol{R}_\mathrm{r}\hat{\boldsymbol{a}})\times\hat{\mathbf{k}}|}$ and $\hat{\boldsymbol{l}}_\mathrm{g} = \hat{\mathbf{k}} \times \hat{\boldsymbol{f}}_\mathrm{g}$. The forces and moments applied by the module on element i are $\boldsymbol{f}_\mathrm{i}$ and $\boldsymbol{m}_\mathrm{i}$, respectively. The radius of the ring is r_r and the mass of the patch is m_p. The point on the ring where residual elements are attached is, $\boldsymbol{p}_\mathrm{r} = \boldsymbol{x}_\mathrm{r} + r_\mathrm{r}\hat{\boldsymbol{l}}_\mathrm{r} \times \hat{\boldsymbol{f}}_\mathrm{r}$. If a vector is expressed as a scalar then its last subscript being 1, 2, or 3 indicate which of its components is meant.

2 Model Implementation

As a continuation of the work of Gualdi *et al.* [7], the model is implemented as a combination of three rigid elements in *MBDyn*. The first is the wheel body, which needs to be connected to an axle or a steering element of the vehicle and allowed to roll. The second is the ring body. It is connected to the wheel through the viscoelastic elements mentioned in the introduction and implemented as reported by Masarati and Morandini [12]. The translational viscoelastic elements between those two bodies act between the ring and a non-rotating element. This non-rotating element is attached to the wheel and shares all of its properties but the rolling rotation. The third rigid element is the patch, which is implemented as a module of *MBDyn* and has its own equations which influence the forces and moments felt by the ring element. This influence is applied to the residual vector which is built and solved by *MBDyn* at each timestep.

2.1 Residual Vector

All the modifications brought to the global residual are given by a vector which has the form $\boldsymbol{\rho} = \begin{bmatrix}\boldsymbol{\rho}_\mathrm{p} & \boldsymbol{\rho}_\mathrm{r}\end{bmatrix}$ and is added to the internal residual vector of the software. Moreover,

$$\boldsymbol{\rho}_\mathrm{p} = \begin{bmatrix} f_{\mathrm{p}1} - \mathrm{m_p}\dot{v}_{\mathrm{p}1} \\ v_{\mathrm{p}1} - \dot{x}_{\mathrm{p}1} \\ f_{\mathrm{p}2} - \mathrm{m_p}\dot{v}_{\mathrm{p}2} \\ v_{\mathrm{p}2} - \dot{x}_{\mathrm{p}2} \end{bmatrix}^\mathrm{T} \quad \boldsymbol{\rho}_\mathrm{r} = \begin{bmatrix} f_{\mathrm{r}1} \\ f_{\mathrm{r}2} \\ f_{\mathrm{r}3} \\ m_{\mathrm{r}1} \\ m_{\mathrm{r}2} \\ m_{\mathrm{r}3} \end{bmatrix}^\mathrm{T} \tag{2}$$

where $\boldsymbol{\rho}_\mathrm{p}$ is the part of the residual vector that defines the dynamic equations of the two degrees of freedom patch and $\boldsymbol{\rho}_\mathrm{r}$ defines the additional forces on the ring body. Although its motion is restrained to two degrees of freedom, the patch is given four lower order degrees of freedom in the module such that the equation $m_\mathrm{p}\ddot{\boldsymbol{x}}_\mathrm{p} + \boldsymbol{f}_\mathrm{p}(\boldsymbol{x}_\mathrm{p}, \dot{\boldsymbol{x}}_\mathrm{p}) = 0$ is rewritten as $m_p\dot{\boldsymbol{v}}_\mathrm{p} + \boldsymbol{f}_\mathrm{p}(\boldsymbol{x}_\mathrm{p}, \boldsymbol{v}_\mathrm{p}) = 0$. The additional degrees of freedom given by $\boldsymbol{v}_\mathrm{p}$ were added in order to have ordinary instead of partial differential equations. Thus, $\boldsymbol{v}_\mathrm{p} = \dot{\boldsymbol{x}}_\mathrm{p}$.

2.2 Jacobian Matrix

The model being implicit, a Jacobian matrix is used to allow convergence of the calculation. The matrix is built to let the solver assess the influence of the modifications to the residual vector on the solution. The idea is to feed the matrix of partial derivatives to the solver. The contribution of the wheel module to the Jacobian matrix is a 10×16 matrix which has the form $\boldsymbol{J} = \begin{bmatrix}\boldsymbol{J}_\mathrm{p} & \boldsymbol{J}_\mathrm{r} & \boldsymbol{J}_\mathrm{w}\end{bmatrix}$ where,

$$\boldsymbol{J}_\mathrm{p} = -\begin{bmatrix} \lambda_{1\mathrm{p}1} & \beta_{1\mathrm{p}1} & \lambda_{1\mathrm{p}2} & \beta_{1\mathrm{p}2} \\ \lambda_{2\mathrm{p}1} & \beta_{2\mathrm{p}1} & \lambda_{2\mathrm{p}2} & \beta_{2\mathrm{p}2} \\ \vdots & \vdots & \vdots & \vdots \\ \lambda_{10\mathrm{p}1} & \beta_{10\mathrm{p}1} & \lambda_{10\mathrm{p}2} & \beta_{10\mathrm{p}2} \end{bmatrix} \tag{3}$$

$$\boldsymbol{J}_\mathrm{r} = -\begin{bmatrix} \beta_{1\mathrm{r}1} & \beta_{1\mathrm{r}2} & \beta_{1\mathrm{r}3} & \gamma_{1r1} & \gamma_{1r2} & \gamma_{1r3} \\ \beta_{2\mathrm{r}1} & \beta_{2\mathrm{r}2} & \beta_{2\mathrm{r}3} & \gamma_{2r1} & \gamma_{2r2} & \gamma_{2r3} \\ \vdots & \vdots & \vdots & \vdots & \vdots & \vdots \\ \beta_{10\mathrm{r}1} & \beta_{10\mathrm{r}2} & \beta_{10\mathrm{r}3} & \gamma_{10r1} & \gamma_{10r2} & \gamma_{10r3} \end{bmatrix} \tag{4}$$

$$\boldsymbol{J}_{\mathrm{w}} = -\begin{bmatrix} \beta_{1\mathrm{w}1} & \beta_{1\mathrm{w}2} & \beta_{1\mathrm{w}3} & \gamma_{1w1} & \gamma_{1w2} & \gamma_{1w3} \\ \beta_{2\mathrm{w}1} & \beta_{2\mathrm{w}2} & \beta_{2\mathrm{w}3} & \gamma_{2w1} & \gamma_{2w2} & \gamma_{2w3} \\ \vdots & \vdots & \vdots & \vdots & \vdots & \vdots \\ \beta_{10\mathrm{w}1} & \beta_{10\mathrm{w}2} & \beta_{10\mathrm{w}3} & \gamma_{10w1} & \gamma_{10w2} & \gamma_{10w3} \end{bmatrix} \tag{5}$$

with the scalars γ_{ijk}, β_{ijk}, and λ_{ijk} given by the following vector equations,

$$\boldsymbol{\gamma}_{ij} = \frac{\partial \rho_i}{\partial \boldsymbol{\omega}_j} + \boldsymbol{\omega}_{ref,j} \times \frac{\partial \rho_i}{\partial \boldsymbol{\omega}_j} d_c + \left(\frac{\partial \rho_i}{\partial (\boldsymbol{R}_j \hat{\boldsymbol{a}})} \times (\boldsymbol{R}_j \hat{\boldsymbol{a}})\right) d_c \tag{6}$$

$$\boldsymbol{\beta}_{ij} = \frac{\partial \rho_i}{\dot{\boldsymbol{x}}_j} + d_c \frac{\partial \rho_i}{\boldsymbol{x}_j} \tag{7}$$

$$\boldsymbol{\lambda}_{ij} = \frac{\partial \rho_i}{\dot{\boldsymbol{v}}_j} + d_c \frac{\partial \rho_i}{\boldsymbol{v}_j} \tag{8}$$

where indices i and k of Eqs. (6) to (8) go from 1 to 10 and 1 to 3, respectively; j can be p, r, or w; the identity $\frac{\partial \rho_i}{\partial \boldsymbol{y}_j} = \left(\frac{\partial \rho_i}{\partial y_{j1}}, \frac{\partial \rho_i}{\partial y_{j2}}, \frac{\partial \rho_i}{\partial y_{j3}}\right)$ is used for the differentiation of a scalar with respect to a vector; and $\boldsymbol{\omega}_{ref,j}$ is the vector of reference angular velocity computed internally by *MBDyn* for element j when solving for a null residual.

From there, the solver is able to search for a solution of the nonlinear system of equations using the Newton-Raphson method. When deriving the Jacobian matrix, the following two properties are used, $\delta y = d_{\mathrm{c}} \delta \dot{y}$ and $\delta g = d_{\mathrm{c}} \delta \dot{g}$. They are a consequence of the use of integrating the problem in time using an implicit integration scheme and a predictor-corrector approach. As a consequence, perturbations of states are proportional to perturbation state derivatives through the d_{c} coefficient, which in turn is proportional to the time step. The force vector is thus iterated to be equal to the multiplication of the Jacobian matrix by the following vector,

$$\begin{bmatrix} \delta \dot{v}_{\mathrm{p}1} & \delta \dot{x}_{\mathrm{p}1} & \delta \dot{v}_{\mathrm{p}2} & \delta \dot{x}_{\mathrm{p}2} & \delta \dot{\boldsymbol{x}}_{\mathrm{r}} & \delta \dot{\boldsymbol{g}}_{\mathrm{r}} & \delta \dot{\boldsymbol{x}}_{\mathrm{w}} & \delta \dot{\boldsymbol{g}}_{\mathrm{w}} \end{bmatrix}^T \tag{9}$$

where

$$\delta \dot{\boldsymbol{x}}_{\mathrm{r}} = \begin{bmatrix} \delta \dot{x}_{\mathrm{r}1} & \delta \dot{x}_{\mathrm{r}2} & \delta \dot{x}_{\mathrm{r}3} \end{bmatrix} \tag{10}$$

$$\delta \dot{\boldsymbol{g}}_{\mathrm{r}} = \begin{bmatrix} \delta \dot{g}_{\mathrm{r}1} & \delta \dot{g}_{\mathrm{r}2} & \delta \dot{g}_{\mathrm{r}3} \end{bmatrix} \tag{11}$$

$$\delta \dot{\boldsymbol{x}}_{\mathrm{w}} = \begin{bmatrix} \delta \dot{x}_{\mathrm{w}1} & \delta \dot{x}_{\mathrm{w}2} & \delta \dot{x}_{\mathrm{w}3} \end{bmatrix} \tag{12}$$

$$\delta \dot{\boldsymbol{g}}_{\mathrm{w}} = \begin{bmatrix} \delta \dot{g}_{\mathrm{w}1} & \delta \dot{g}_{\mathrm{w}2} & \delta \dot{g}_{\mathrm{w}3} \end{bmatrix} \tag{13}$$

where $\delta\dot{\boldsymbol{x}}_i$, $\delta\dot{\boldsymbol{v}}_i$, and $\delta\dot{\boldsymbol{g}}_i$ represent the increments between the previous and current iterations of the derivatives of the position, velocity, and rotation parameter, respectively, of element i. A more complete description of the integration methods used in *MBDyn* is given by Masarati [10, 11].

2.3 Forces and Moments

The carcass elements are taken into account by *MBDyn* with a standard 6 DoF viscoelastic connection. In the developed module, three moments and two forces are applied to the ring node. Two forces are applied to the patch.

The ring moments consist of the quasi-static portion of the aligning torque due to the tire construction and its unequal pressure distribution along its longitudinal axis; the moment caused by the variable position of the patch, which is where the forces are applied; and the rolling resistance moment.

The ring forces are the centripetal force and the interaction force induced by the residual elements. The patch forces are the interaction force and the slip forces.

The module's forces and moments are thus,

$$\boldsymbol{f}_\mathrm{p} = \boldsymbol{f}_\mathrm{s} - \boldsymbol{f}_\mathrm{i} \tag{14}$$

$$\boldsymbol{f}_\mathrm{r} = \boldsymbol{f}_\mathrm{ir} + \boldsymbol{f}_\mathrm{c} \tag{15}$$

$$\boldsymbol{m}_\mathrm{r} = \boldsymbol{d} \times (\boldsymbol{f}_\mathrm{ir} + \boldsymbol{f}_\mathrm{d}) + \boldsymbol{m}_\mathrm{z} \tag{16}$$

where each variable will be defined in what follows.

2.4 Slip Forces

The friction forces between the road and tire are computed from an adaptation of the well known Pacejka magic formulae [16]. The equations were fitted to 2800 kg nominal load experimental force curves provided by Michelin.

First, some quantities are defined. In the module, the patch follows the ring in position but not in rotation, thus the patch reverse velocity vector has to be defined as,

$$\boldsymbol{\nu}_\mathrm{p} = -\boldsymbol{\omega}_\mathrm{r} \times \boldsymbol{d} - (\boldsymbol{v}_\mathrm{p} - \boldsymbol{v}_\mathrm{w}) \tag{17}$$

where the distance from center of ring to patch is,

$$\boldsymbol{d} = -\hat{\boldsymbol{n}} r_{\mathrm{r}} + \boldsymbol{x}_{\mathrm{p}} - \boldsymbol{p}_{\mathrm{r}} \tag{18}$$

It is now possible to express the slip ratio as,

$$\kappa = \hat{\boldsymbol{f}}_{\mathrm{w}} \cdot \frac{\boldsymbol{v}_{\mathrm{w}} - \boldsymbol{\nu}_{\mathrm{p}}}{\left| \hat{\boldsymbol{f}}_{\mathrm{w}} \cdot \boldsymbol{v}_{\mathrm{w}} \right|} \tag{19}$$

and the slip angle as,

$$\alpha = \arctan \frac{\hat{\boldsymbol{l}}_{\mathrm{w}} \cdot \boldsymbol{v}_{\mathrm{w}}}{\left| \hat{\boldsymbol{f}}_{\mathrm{w}} \cdot \boldsymbol{v}_{\mathrm{w}} \right|} \tag{20}$$

which give the longitudinal and lateral slip forces, respectively as,

$$f_\kappa = D_\kappa sin\Big(C_\kappa \arctan\Big(B_\kappa \alpha - E_\kappa \big(B_\kappa \alpha - \arctan\left(B_\kappa \alpha\right)\big)\Big)\Big) + S_{\mathrm{V}\kappa} \tag{21}$$

and

$$f_\alpha = D_\alpha sin\Big(C_\alpha \arctan\Big(B_\alpha \kappa - E_\alpha \big(B_\alpha \kappa - \arctan\left(B_\alpha \kappa\right)\big)\Big)\Big) + S_{\mathrm{V}\alpha} \tag{22}$$

The residual moment is,

$$M_{\mathrm{zr}} = G_{\mathrm{t}} \cos\Big(\arctan\big(H_{\mathrm{t}}(\tan\alpha + S_{\mathrm{Hf}})\big)\Big) \tag{23}$$

and the pneumatic trail is,

$$p_{\mathrm{t}} = -D_{\mathrm{t}} \cos\Big(C_{\mathrm{t}} \arctan\big(F_{\mathrm{t}} - E_{\mathrm{t}}(F_{\mathrm{t}} - \arctan F_{\mathrm{t}})\big)\Big) \tag{24}$$

where $F_{\mathrm{t}} = B_{\mathrm{t}}(\tan\alpha + S_{\mathrm{Ht}})$. Finally, B_{i}, C_{i}, D_{i}, E_{i}, G_{i}, H_{i}, S_{Vi}, S_{Hf}, and S_{Ht} are coefficients proper to each tire. Those coefficients are found by fitting the equations to the experimental by means of a minimization procedure. For the aligning torque, the pneumatic trail and residual moment are both obtained from a single experimental curve which gives only the total moment. Thus, the S_{Hf} parameter was first found by taking the zero of the f_α function.

The fitted curves are shown in Fig. 2 along with the experimental data at various loads other than the one used for calibration.

The slip forces can now be expressed as,

$$\boldsymbol{f}_{\mathrm{s}} = -(f_\alpha \hat{\boldsymbol{l}}_{\mathrm{w}} + f_\kappa \hat{\boldsymbol{f}}_{\mathrm{w}}) f_{\mathrm{p3}} \tag{25}$$

and the aligning torque as,

$$\boldsymbol{m}_{\mathrm{z}} = \hat{\boldsymbol{n}}(-p_{\mathrm{t}} f_{\mathrm{r2}} + M_{\mathrm{zr}}) \tag{26}$$

The slip forces are applied to the patch. The aligning torque is applied directly on the ring and takes the lateral component of the interaction force as input force.

The slip velocity of the patch is used in lieu of relying on an effective radius method.

Finally, for Eq. (19), if $|\boldsymbol{f}_{\mathrm{w}} \cdot \boldsymbol{v}_{\mathrm{w}}|$ becomes smaller than a threshold value, it is incremented by a small value while preserving its sign. The resulting κ is capped to a threshold value. The inverse tan function used in Eq. (20) is a builtin c++ function that forces the output to be in the first two quadrants and will not diverge when the denominator is null.

2.5 Viscoelastic Forces

The residual elements are handled by the c++ module. These six viscoelastic elements produce the interaction force vector defined as the sum of the elastic and viscous forces, respectively as,

$$\boldsymbol{f}_{\mathrm{i}} = \boldsymbol{f}_{\mathrm{e}} + \boldsymbol{f}_{\mathrm{v}} \tag{27}$$

where

$$\begin{bmatrix} \boldsymbol{f}_{\mathrm{e}} \\ \boldsymbol{f}_{\mathrm{v}} \end{bmatrix} = \begin{bmatrix} \boldsymbol{x}_{\mathrm{p}} - \boldsymbol{p}_{\mathrm{r}} \\ \boldsymbol{v}_{\mathrm{p}} - \boldsymbol{v}_{\mathrm{r}} \end{bmatrix} \begin{bmatrix} \hat{\boldsymbol{f}}_{\mathrm{g}}^{\mathrm{T}} & \hat{\boldsymbol{l}}_{\mathrm{g}}^{\mathrm{T}} & \hat{\mathbf{k}}^{\mathrm{T}} \end{bmatrix} \odot \begin{bmatrix} \boldsymbol{k}_{\mathrm{r}} \\ \boldsymbol{c}_{\mathrm{r}} \end{bmatrix} \tag{28}$$

where $\boldsymbol{k}_{\mathrm{r}}$ et $\boldsymbol{c}_{\mathrm{r}}$ are the stiffness and damping vectors of the residual elements, respectively. The interaction force $\boldsymbol{f}_{\mathrm{i}}$ is rotated before being applied on the ring,

$$\boldsymbol{f}_{\mathrm{ir}} = \begin{bmatrix} -\hat{\boldsymbol{n}} \times \hat{\boldsymbol{a}} & \hat{\mathbf{j}} & \hat{\boldsymbol{n}} \end{bmatrix} \cdot \boldsymbol{f}_{\mathrm{i}} \tag{29}$$

2.6 Centrifugal Force

The centrifugal force slightly increases the radius of a tire. In the model, the radius is increased by the application of a force on the ring. That force has no effect on the patch and is calculated assuming a steady-state condition. The force equation is,

$$\boldsymbol{f}_{\mathrm{c}} = \hat{\boldsymbol{n}} \frac{k_{\mathrm{p3}}}{k_{\mathrm{r3}}} r_{\mathrm{r}} r_{\mathrm{a}} (m_{\mathrm{r}} + m_{\mathrm{p}}) (\hat{\boldsymbol{f}}_{\mathrm{r}} \cdot \boldsymbol{\omega}_{\mathrm{r}} \times \hat{\boldsymbol{n}})^2 \tag{30}$$

where r_a is the approximate ratio of the patch length to the ring circumference. The angular ring velocity is converted into a linear one. An explanation is given in Fig. 3 where the ring and patch are bundled for the computation of a centrifugal force that is then converted to an equivalent centripetal force. It acts on the ring and causes the same radius increase as the centrifugal force would.

2.7 Rolling Resistance

This resistance is calculated using an empirical formula given by Pacejka [16] and is applied as a moment on the ring,

$$\boldsymbol{f}_d = \hat{\boldsymbol{f}}_r f_{p3} \left(q_a + q_b \left| \frac{\hat{\boldsymbol{f}}_w \cdot \boldsymbol{v}_w}{v_o} \right| \right) \operatorname{sgn} \left(\hat{\boldsymbol{f}}_w \cdot \frac{\boldsymbol{\omega}_w \times \hat{\mathbf{k}}}{\hat{\boldsymbol{f}}_w \cdot \boldsymbol{v}_w} \right) \tag{31}$$

where q_i are empirically obtained parameters and v_o is the reference velocity used during the measurements.

2.8 The Artificial Rotations

The patch element has two translational degrees of freedom and inherits its angular position from the ring body. Its longitudinal and lateral directions are assumed to always be along $\hat{\boldsymbol{f}}_r$ and $\hat{\boldsymbol{l}}_r$, respectively. Thus, its vertical plane is always perpendicular to the road normal direction, $\hat{\boldsymbol{n}}$. The interpretation of this rotation is shown in Fig. 4 and the effects of its implementation is seen in Eqs. (26), (29) and (39).

Also, an additional element with no mass is added between the wheel and axle and this element does not rotate with the wheel other than for steering. This element is where carcass elements connect to the wheel.

2.9 Contact Patch Length

Contact lengths of the test tire under different loads were gathered from finite element analyses provided by Michelin and the equation proposed by Besselink [2] was fitted to that data,

$$L_s = c_a r_r \left(\frac{\delta\, r}{r_r} + c_b \sqrt{\frac{\delta\, r}{r_r}} \right) \tag{32}$$

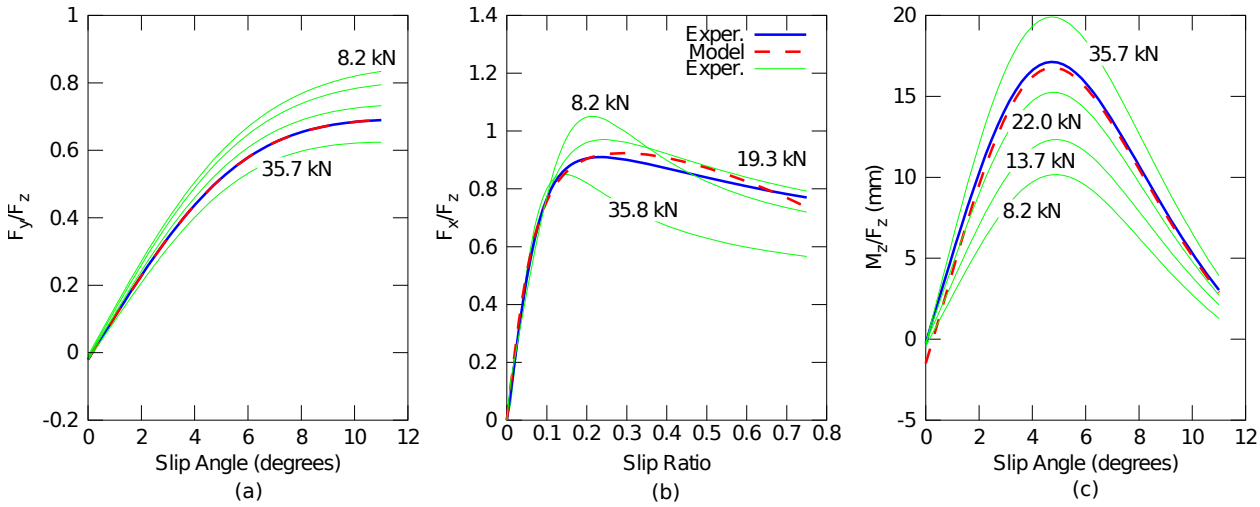

Figure 2: Experimental and model data for slip forces at 2800 kg load. Experimental data at different loads is shown in pale. a) Lateral force, b) longitudinal force, and c) aligning moment.

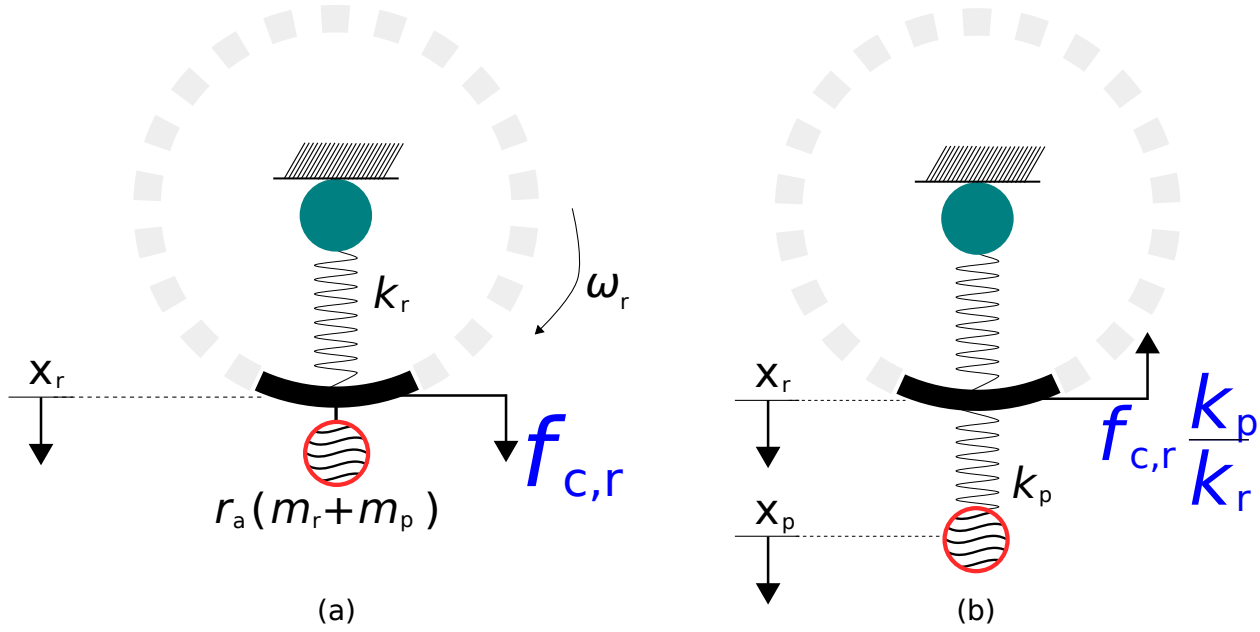

Figure 3: Systems used to a) compute, and b) apply, the rotation induced forces.

where c_i are the coefficients used to fit the equation and $\delta\ r$ is the deflection of the tire in the normal direction. Figure 5 shows the data points from Michelin along with the curves obtained from Eq. (32) using a) the coefficients suggested by Besselink for a car, b) the ones fitted to the data from Michelin, and c) the same coefficients but with $\frac{\delta\ r}{r_\mathrm{r}}$ removed from the equation.

2.10 Road Profile

The model takes the exact longitudinal road profile as input and filters it according to a method inspired by the one put forward by Schmeitz [19]. The input profile is filtered twice: once using a GNU Octave [4] ellipse filter script prior to feeding it to the module and once within the module itself. After the filtering, the resulting profile dictates the patch height and slope. The model assumes the patch to be attached to the road and the normal force is not allowed to become smaller than zero.

2.10.1 Superellipse

The ellipse based filtering is done by finding the height of the bottommost point of a superellipse that travels on a given longitudinal profile. The filter yields the relative height increase, z_e, caused by the intersection of the ellipse with the surrounding profile,

$$z_\mathrm{e} = \begin{cases} 0 & \text{if } x_\mathrm{i} <= x_\mathrm{s} - l_\mathrm{b} \\ h_\mathrm{s} - b_\mathrm{e} + \left| b_\mathrm{e} \left(1 - \left(\frac{|x_\mathrm{i} - x_\mathrm{s}|}{a_\mathrm{e}} \right)^{c_\mathrm{e}} \right)^{1/c_\mathrm{e}} \right| & \text{if } x_\mathrm{s} - l_\mathrm{b} < x_\mathrm{i} < x_\mathrm{s} \\ h_\mathrm{s} & \text{if } x_\mathrm{i} >= x_\mathrm{s} \end{cases} \tag{33}$$

where x_i is the possibly intersecting point considered and,

$$l_\mathrm{b} = a_\mathrm{e} \left(1 - \left(1 - \frac{|h_\mathrm{s}|}{b_\mathrm{e}} \right)^{c_\mathrm{e}} \right)^{1/c_\mathrm{e}} \tag{34}$$

where h_s is the difference in height between the current position and x_i; and a_e, b_e, and c_e are the superellipse parameters. The equations shown only look at the possibly intersecting points ahead of the ellipse; a similar equation takes care of the points behind and the highest of the two results is retained. Finally, the height of the ellipse filtered profile is,

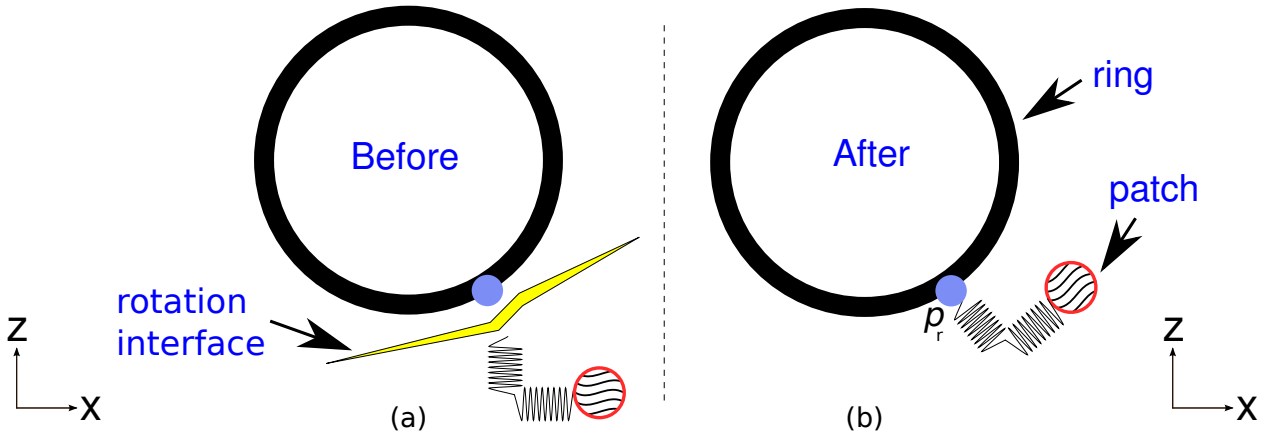

Figure 4: a) As written in the residual vector, and b) as modeled with the artificial rotation.

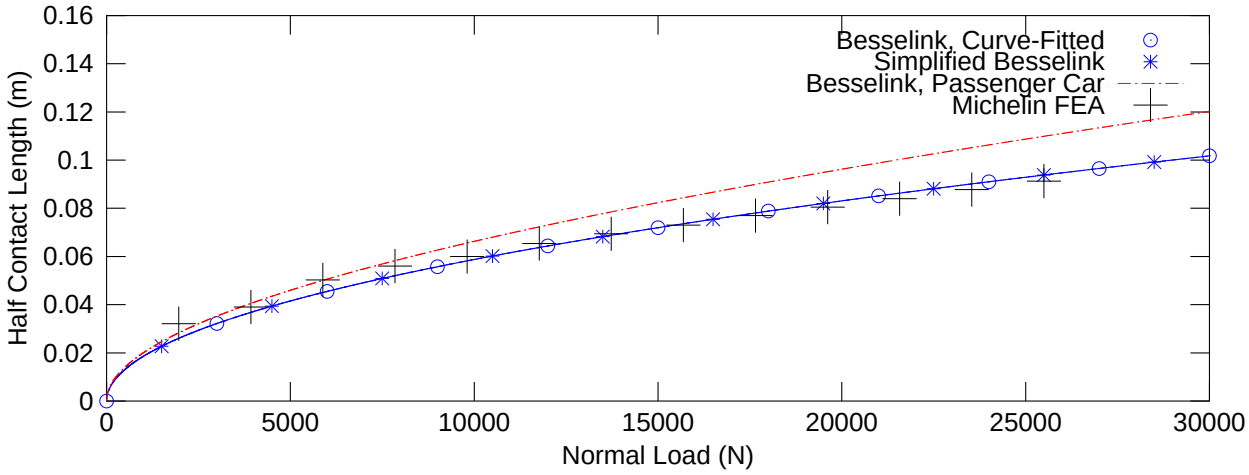

Figure 5: Comparison of different contact length equations with the data from Michelin.

$$x_{p3} = z_o + z_e \tag{35}$$

where z_o is the height of the unfiltered profile at the point considered.

The ellipse was tuned to match the side view of a loaded tire, as recommended by Schmeitz [19]. The side view was generated using analytical formulae by Rhyne [18]. Rhyne assumes that the tire belt is inextensible. His formulae return a tire shape which is a perfect circle when unloaded. Under load, there is a flat zone of contact with the ground, a counter deflection at the free contour of the tire to offset for the radius reduction at the flat zone, and a transition zone in between the flat and free zones which is a circle centered vertically above the point of loss of contact with the ground. Figure 6 shows the contour of the tire calculated using the formulae by Rhyne and using the superellipse shape both with parameters suggested by Schmeitz and with those fitted to the Rhyne contour.

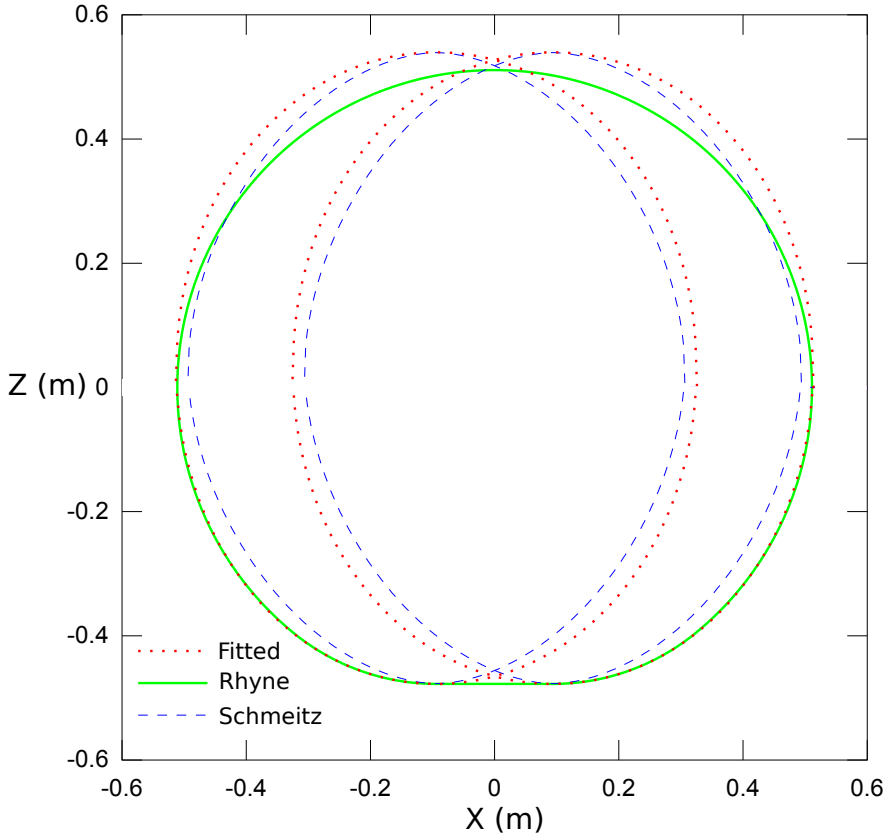

Figure 6: Fitting the Schmeitz superellipse to the Rhyne sidewall shape.

2.10.2 Two-Point Follower

The ellipse filtered road profile is fed to the tire module, where a two-point follower technique is used. It consists of finding the front and rear edges of the contact zone by applying a load-dependent offset to the longitudinal patch position. The line that connects the front and read edges yields the height and normal direction of the patch.

The two-point follower technique thus yields the following normal direction and height,

$$\boldsymbol{n} = \left(\left[x_{\mathrm{p1}+}, 0, x_{\mathrm{p3}+}\right] - \left[x_{\mathrm{p1}-}, 0, x_{\mathrm{p3}-}\right]\right) \times \hat{\boldsymbol{a}} \tag{36}$$

$$x_{\mathrm{p3}} = \frac{x_{\mathrm{p3}+} + x_{\mathrm{p3}-}}{2} \tag{37}$$

where

$$x_{\mathrm{p3}\pm} = x_{\mathrm{p3}}(x_{\mathrm{p1}} = x_{\mathrm{p1}\pm} = x_{\mathrm{p1}} \pm l_{\mathrm{s}}) \tag{38}$$

is taken directly from the ellipse filtered profile data and the half length of the patch projected on the longitudinal axis of the road profile is,

$$l_{\mathrm{s}} = \hat{\boldsymbol{f}}_{\mathrm{r}} \cdot \hat{\mathbf{i}} L_{\mathrm{s}} P_{\mathrm{s}} \tag{39}$$

where P_{s} is the ratio between patch and two point follower lengths.

2.11 Variable Time Step

In order to shorten the time required to calibrate the model to Michelin's finite element data, a timestep controller algorithm was implemented in the tire model. The timestep adjustment is calculated at the start of a timestep iteration and applied to the following timestep. This section briefly describes the algorithm. It is tuned by user parameters such as those described in Table 1.

Table 1: Some parameters used by the variable timestep algorithm.

dt_{mH}	maximum desired profile height change over one timestep
d_{mx}	maximum timestep allowed
d_{mn}	minimum timestep allowed
d_{mf}	maximum division of timestep size per timestep
d_r	resolution by which to scan the road profile

The algorithm scans the road profile in front of the vehicle at a distance closely equal to the total distance traveled by the patch to go from the maximum to the minimum timestep sizes by decrements of d_{mf} per timestep. This distance is,

$$d_a = \sum_{i=0}^{\left\lceil \frac{log(d_{mx}/d_{mn})}{log\left(d_{mf}\right)} \right\rceil} \frac{\delta x_{\mathrm{p1}}}{(d_{mf})^i} \tag{40}$$

where $\lceil\ \rceil$ denotes the ceiling function and δx_{p1} is the change in road profile longitudinal position between the current and previous timesteps. From this, the number of steps to take in the profile scanning procedure is computed as,

$$d_n = \left\lceil \frac{d_a}{d_r} \right\rceil \tag{41}$$

and for each of those steps every possible contact point is examined. The difference between the maximum and minimum ground heights encountered is retrieved as d_H. From this, the division required to the current timestep size to accommodate the upcoming deformation is,

$$d_f = \frac{d_H}{dt_{mH}} \tag{42}$$

and may be larger than the maximum allowed division. Thus, with equations very similar to Eqs. (40) and (41), a distance over which the desired timestep change will be applied is computed. Then, the upcoming timestep is decreased, increased, or left intact. At each timestep, the timestep size change is limited according to the upper and lower boundaries for both the value and change of timestep allowed.

A second check looks at the interaction force. It monitors how many sign changes occurred over the last given number of steps and modifies the timestep accordingly.

In the end the most restrictive condition, either from an upcoming road deformation or from force oscillations, is applied to the model.

3 Calibration and Validation

Available experimental data from static tests and steady state friction force curves combined with rules of thumb by Pacejka [16] and other assumptions were used to yield a first set of model parameters. The model behavior using these parameters can be seen in Fig. 7.

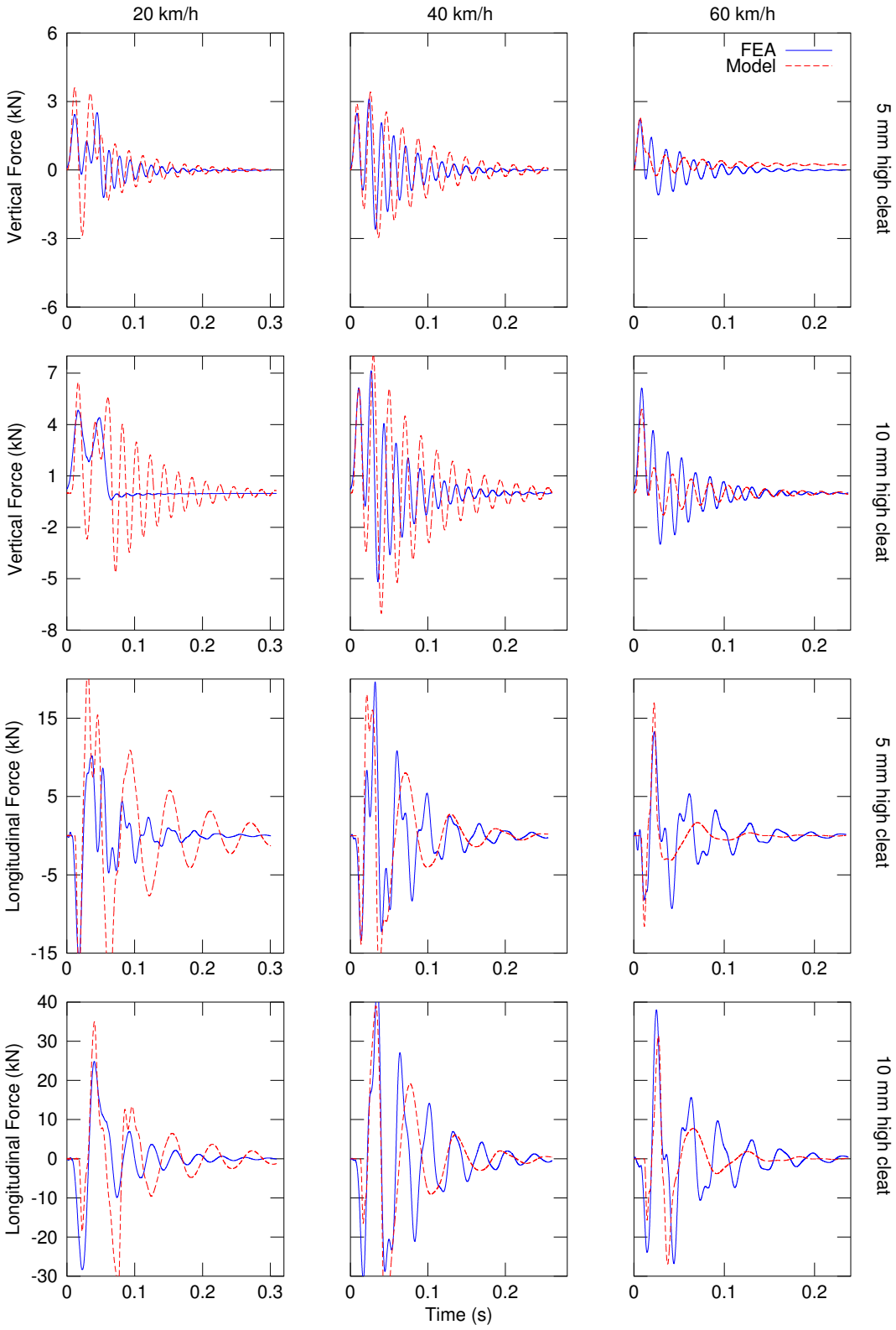

Figure 7: Force variations felt at the axle while traveling on a flat road and running into a 20 mm long rectangular cleat. Axle height fixed at a 27.47 kN static normal load. Initial parameters.

After these initial tests, the output of finite element analyses (FEA), provided by Michelin and calibrated to experimental data, of a tire mounted on an axle and rolled over rectangular cleats at different velocities and a constant axle loading of 27.47 kN were used to calibrate the model. A Nelder-Mead optimization algorithm [6] was used into a loop of simulations that varied 24 model parameters consisting mainly of the stiffness and damping properties of the tire; the mass and angular mass distributions between wheel, ring, and patch; and, the contact length and the superellipse parameters. The evaluation of the quality of the results was a weighted error function using the coefficient of determination defined by,

$$R^2 = 1 - \frac{\sum_i (\zeta_i - \eta_i)^2}{\sum_i (\zeta_i - \overline{\zeta})^2} \tag{43}$$

where ζ and η are the force curves calculated by the Michelin FEA and by the developed model, respectively, and $\overline{\zeta}$ is the average of ζ. The coefficients of determination obtained are given in Table 2. They were then weighted to give more importance to the velocity of 60 km/h and the longitudinal forces. The weighting factors ξ used on R^2 are given in Table 2. The objective function minimized by the Nelder-Mead algorithm is,

$$\sum_{j=1}^{12} \left(\xi_j \left(1 - R_j^2 \right) \right) \tag{44}$$

Table 2: Coefficients of determination before and after calibrating the model.

v_{w1} (km/h)	20				40				60			
h (mm)	5		10		5		10		5		10	
Force	x	z	x	z	x	z	x	z	x	z	x	z
R^2, initial	-2.4	-1.0	-.0062	-.69	-.14	-1.0	0.32	-1.3	0.50	0.20	0.40	0.44
R^2, optim.	0.15	0.53	0.73	0.32	0.51	0.80	0.56	0.85	0.55	0.85	0.56	0.88
Weight ξ	0.25	0.25	0.25	0.25	0.55	0.55	0.55	0.55	5	1	5	1

After being optimized, the comparison with the data provided by Michelin is conclusive, as can be seen from Table 2 and Fig. 8.

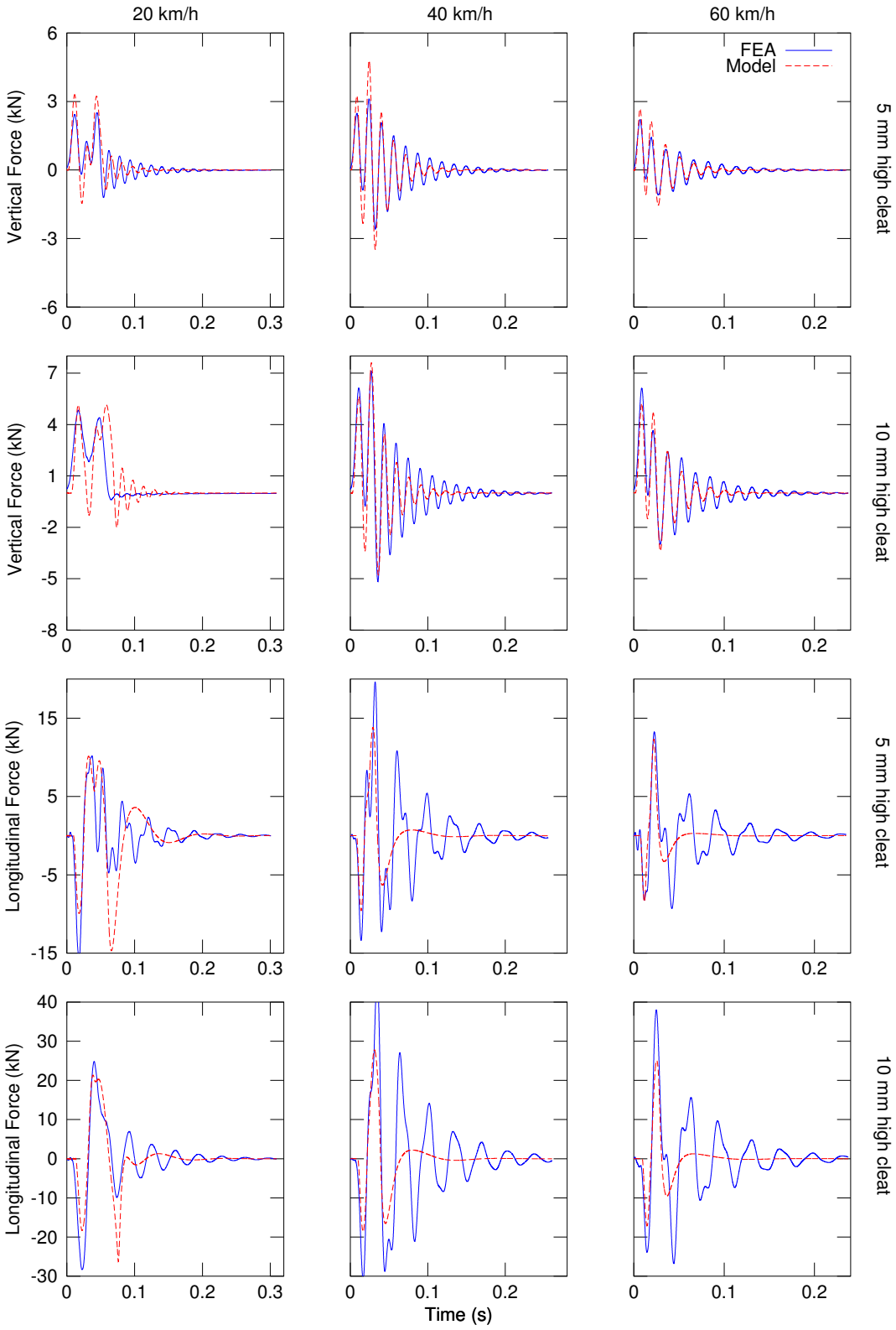

Figure 8: Force variations felt at the axle while traveling on a flat road and running into a 20 mm long rectangular cleat. Axle height fixed at a 27.47 kN static normal load. Optimized parameters.

4 Discussion

4.1 Model Peculiarities

The artificial rotation assumption and the absence of gravity acting on the patch are reasonable in the sense that this element is not a physical body. It is only a mass used to model the delay of the response and the displacement of the tread under dynamic loading. To exhibit a dynamic delay, the aligning torque equation takes the interaction force as input instead of the lateral slip force. Finally, the non rolling element attached to the wheel prevents *MBDyn* from interpreting coefficients of damping and stiffness in the relative reference frame of the wheel which rotates as it rolls.

The interaction force acts on the ring at the position of the patch. This models the dynamic part of the aligning and rolling resistance moments. It also makes the steady-state rolling resistance moment influence itself by the extension it causes in the residual elements. Thus, the rolling resistance coefficient could be calibrated to make sure that the measured rolling resistance is respected. Other than by that effect, the steady state rolling resistance is not taken into account by the residual elements because they do not roll with the wheel and are thus not periodically deformed by an intermittent contact with the ground. By assuming that most of the energy dissipation occurs in the area of the patch, the rolling resistance was made to act along the ring rather than the wheel. The velocity component of the rolling resistance equation was not used in the results shown and high velocity phenomena such as standing waves are disregarded altogether by the model because they are negligible at the velocities of interest [25].

The S_{Hf} shift ensured that the maximum residual torque value occurs at the point of null lateral force, as outlined by Pacejka [16]. The centrifugal force increases the radius of a Formula SAE tire by 0.75% at 100 km/h [14] and has an effect within the model that is noticeable only by numerical comparison of the results. That force was nonetheless maintained. The variable timestep feature turns out to be most useful with punctual surface irregularities. When calibrating the model to the cleat response data, the timestep oscillated between 2×10^{-5} s and 1×10^{-2} s which allowed the tests to complete seven times faster without reducing accuracy. The variable timestep algorithm does not scan the road profile behind the current road position because the model is aimed at forward movement. Furthermore, a small move rearwards would be taken care by the safety factor of the deformation search. To ensure initial stability, the stiffnesses and dampings used

in the model can be defined by a time dependent function.

To remain simple, the model uses an approximate Jacobian matrix. This has no effect on the precision of the calculation because that matrix is only used while searching for a solution to the residual vector. A more precise Jacobian matrix usually improves convergence time but not precision. Every equation, including the slip forces, is integrated implicitly and the only exception is x_{p1} of Eq. (38) which is taken from the previous timestep. If it were made implicit, the calculation of its derivative would need a particular treatment since it is discontinuous at every point.

The assumption of continuous road-tire contact is deemed appropriate for the intended range of application. The wheel state is used as input to Eqs. (19) and (20) because this is where the data was read during experimental tests.

The effective rolling radius is defined differently by various authors and visibly no consensus has been reached yet [22, 21, 2, 16, 25]. It thus was chosen to take the physically sound approach of measuring slip directly from the patch velocity.

As was seen in Fig. 5, Eq. (32) could have been simplified without any loss of accuracy. In that same equation, Besselink used the vertical tire deflection on his perfectly smooth roads but here the normal direction is used for exactness.

The road profile is filtered because Schmeitz [19] states that the front and rear tire contours near the ground are described by two identical rigid superellipses and the contact zone by a load-dependent line which connects them. The ellipse filter is applied using GNU Octave because it is only necessary to apply the ellipse filter once per profile. The filter based distance between the two edges of the tire must be applied during the simulation because it depends on the normal load. Finally, a vertical load close to the expected operating condition was used when fitting the superellipse to the formulae by Rhyne [18] because they generate different shapes under different loads.

4.2 Aspects of the Calibration

The first attempt at calibration was done manually by trying to reproduce the different modes observed in the FEA and tuning the parameters to match natural frequencies and dampings. The method turned out to be impractical when tuning the model to the 12 different test cases considered.

It was also considered to calibrate the model based on the energy losses induced by the cleat on the tire, but the FEA was not complete enough energy-wise. It gives

the longitudinal forces as differences from the mean, the time lapse does not reach settlement of the force oscillations, and the location of the cleat at time zero is unknown. Such small cleats also have minimal impacts on energy dissipation.

The calibration approach used is deemed appropriate because Schmeitz and Versteden [20] declared that a combination of quasi static experiments and cleat tests allows a good calibration of rigid ring models. The method of Schmeitz [19] consisted of finding the optimal set of parameters for each operating condition and then averaging these parameters to yield a global set of parameters. In doing so, he concentrated on representing individual natural frequencies properly. Here, a strong emphasis was put on the energy dissipation which is why the optimization process was designed to have the best overall match of high velocity longitudinal force curves.

4.3 Validity and Accuracy

Fig. 2 showed that divergences in normalized slip forces for different loads increase with slip ratio. This is not an issue at the small and unidirectional slips at loads close to 2800 kg that are expected in the project. Nevertheless, the model is also able to handle curved paths and strong accelerations.

Schmeitz reports that his rigid ring model behaves accurately for sudden deformations of up to 10 cm and at frequencies under 100 Hz, above which flexible ring modes that cannot be represented by a rigid ring model become too important. A similar range of validity is assumed for the current model.

The quality of the results obtained with the calibrated model is similar to what was presented by Maurice [13] and Zegelaar [25] and better than those presented by Frey [5]. Schmeitz [19] however, does present a better longitudinal force calculation for some of his triangular cleat tests. One can assume that the 14 cases he selected are the best out of the 72 conditions he used for validation, but this explanation is not enough. Another explanation could be the different effective rolling radius used by both Schmeitz and Zegelaar, but again the later did not display such precise results as the former. Another hypothesis is the different approach used for optimization of the parameters. In brief, more conditions will need to be tested before the longitudinal accuracy can be assessed.

4.4 Module within a Semi-Trailer

The resolution of the road profile used for the cleat tests was 1 mm whereas when part of a full semi-trailer simulation, the tire model behaved as expected for road readings taken at 1 cm intervals. When part of a full vehicle model, the timestep from the most restrictive wheel is applied to the whole multibody model. The module allows looping over a specific part of interest of a profile and setting an initial buffer zone where the model slowly reaches the initial height of the input profile. In situations where the 22-wheel truck travels over a constantly rough road, the variable timestep algorithm is too slow and it is more appropriate to rely on a constant timestep. The details of the implementation within a semi-trailer model will be discussed in an upcoming article.

5 Conclusion

This model is made available as part of the *MBDyn* multibody dynamics package [1] and one is encouraged to look at its source code to grasp a deeper understanding. It is expected to be accurate under excitation frequencies up to 100 Hz and road deformation up to 10 cm. It takes 45 tire parameters and 20 algorithm parameters and is integrated implicitly except for the road profile. The model has been calibrated and validated against a trusted finite element analysis of Michelin XZA-3 tires mounted on a wheel and axle assembly going over rectangular cleats. Over 20 km/h, R^2 was above 0.8 for every test of the vertical force response to cleats. As for the longitudinal forces, only one curve had a R^2 below 0.5. A variable timestep algorithm was also included in the module and found to reduce the simulation time of the test cases by 85%.

Future work includes an experimental validation on a real road which would lead to a model recalibration and possible refinements such as using non-linear or frequency dependent springs and dampers.

6 Aknowledgements

We would like to thank François Beauchamps, Erin McMullin, Jeff Pyle, Jeff Reno, and Anton Thomas of Michelin North America for providing useful data and feedback for the model; Vincenzo d'Alessandro of Politecnico di Milano for

helping with the development of the model; Compute-Canada for providing computer facilities; and the i3C research chair for creating the project.

References

[1] MBDyn 1.5 source code. `www.mbdyn.org`, 2012.

[2] I. J. M. Besselink. *Shimmy of aircraft main landing gears*. PhD thesis, Delft University of Technology, 2000.

[3] C. Canudas de Wit and P. Tsiotras. Dynamic tire friction models for vehicle traction control. *Proceedings of the 38th IEEE Conference on Decision and Control*, 4:3746–3751, 1999.

[4] J. W. Eaton, D. Bateman, and S. Hauberg. *GNU Octave : a high-level interactive language for numerical computations ; edition 3 for Octave version 3.0.2, August 2008*. Network Theory Ltd., October 2008.

[5] N. W. Frey. Development of a rigid ring tire model and comparison among various tire models for ride comfort simulations. Master's thesis, Clemson University, 2009.

[6] E. Grossmann. Nelder-mead minimization from optim-1.0.10. `octave.sourceforge.net`, 2008.

[7] S. Gualdi, M. Morandini, and G. L. Ghiringhelli. Anti-skid induced aircraft landing gear instability. *Aerospace Science and Technology*, 12(8):627–637, 2008.

[8] J. R. Allen II. Rigid ring quarter-vehicle model for durability and ride comfort predictions. Master's thesis, Pennsylvania State University, 2007.

[9] J. W. L. H. Maas. A comparison of dynamic tyre models for vehicle shimmy stability analysis. Master's thesis, Eindhoven University of Technology, 2009.

[10] P. Masarati. *Comprehensive Multibody AeroServoElastic Analysis of Integrated Rotorcraft Active Controls*. PhD thesis, Politecnico di Milano, 2000.

[11] P. Masarati. *MBDyn Theory and Developer's Manual Version 1.X-Devel*. Politecnico di Milano, 2010.

[12] P. Masarati and M. Morandini. Intrinsic deformable joints. *Multibody System Dynamics*, 23(4):361–386, 2010.

[13] J. P. Maurice. *Short Wavelength and Dynamic Tyre Behaviour under Lateral and Combined Slip Conditions*. PhD thesis, Delft University of Technology, 2000.

[14] Michelin. Formula SAE tire data, 2009.

[15] A. J. P. Miege and A. A. Popov. The rolling resistance of truck tyres under a dynamic vertical load. *Vehicle System Dynamics*, 43:135–144, 2005.

[16] H. B. Pacejka. *Tire and vehicle dynamics*. Society of Automotive Engineers, 2006.

[17] A. A. Popov, D. J. Cole, C. B. Winkler, and D. Cebon. Laboratory measurement of rolling resistance in truck tyres under dynamic vertical load. *Proceedings of the Institution of Mechanical Engineers, Part D: Journal of Automobile Engineering*, 217:1071–1079, 2003.

[18] T.B. Rhyne. Development of a vertical stiffness relationship for belted radial tires. *Tire Science and Technology*, 33(3):136–155, 2005.

[19] A. J. C. Schmeitz. *A Semi-Empirical Three-Dimensional Model of the Pneumatic Tyre Rolling over Arbitrarily Uneven Road Surfaces*. PhD thesis, Delft University of Technology, 2004.

[20] A. J. C. Schmeitz and W. D. Versteden. Structure and parameterization of mf-swift, a magic formula-based rigid ring tire model. *Tire Science and Technology*, 37(3):142–164, 2009.

[21] R. F. Smiley and W. B. Horne. Mechanical properties of pneumatic tires with special reference to modern aircraft tires. Technical report, National Advisory Committee for Aeronautics, 1958.

[22] V. V. Vantsevich, D. Barz, and J. Kubler. Tire longitudinal elasticity and effective rolling radii: experimental method and data. Technical report, Kistler Instrumente AG, 2005.

[23] S. A. Velinsky and R. A. White. Vehicle energy dissipation due to road roughness. *Vehicle System Dynamics*, 9:359–384, 1980.

[24] H. Wang, I. I. Al-Qadi, and I. Stanciulescu. Simulation of trye-pavement interaction for predicting contact stresses at static and various loading conditions. *International Journal of Pavement Engineering*, 13(4):310–321, 2012.

[25] P. W. A. Zegelaar. *The Dynamic Response of Tyres to Brake Torque Variations and Road Unevennesses*. PhD thesis, Delft University of Technology, 1998.